Radboud Repository

Radboud University Nijmegen

PDF hosted at the Radboud Repository of the Radboud University Nijmegen

The following full text is a publisher's version.

For additional information about this publication click this link.
http://hdl.handle.net/2066/125474

Please be advised that this information was generated on 2017-12-06 and may be subject to change.

Functional and Structural Neural Network Characterization of Serotonin Transporter Knockout Rats

Kajo van der Marel[1]*, **Judith R. Homberg**[2], **Willem M. Otte**[1,3], **Rick M. Dijkhuizen**[1]

1 Biomedical MR Imaging and Spectroscopy Group, Image Sciences Institute, University Medical Center Utrecht, Utrecht, The Netherlands, 2 Department of Cognitive Neuroscience, Centre for Neuroscience, Donders Institute for Brain, Cognition, and Behaviour, Radboud University Nijmegen Medical Centre, Nijmegen, The Netherlands, 3 Department of Pediatric Neurology, Rudolf Magnus Institute of Neuroscience, University Medical Center Utrecht, Utrecht, The Netherlands

Abstract

Brain serotonin homeostasis is crucially maintained by the serotonin transporter (5-HTT), and its down-regulation has been linked to increased vulnerability for anxiety- and depression-related behavior. Studies in 5-HTT knockout (5-HTT$^{-/-}$) rodents have associated inherited reduced functional expression of 5-HTT with increased sensitivity to adverse as well as rewarding environmental stimuli, and in particular cocaine hyperresponsivity. 5-HTT down-regulation may affect normal neuronal wiring of implicated corticolimbic cerebral structures. To further our understanding of its contribution to potential alterations in basal functional and structural properties of neural network configurations, we applied resting-state functional MRI (fMRI), pharmacological MRI of cocaine-induced activation, and diffusion tensor imaging (DTI) in 5-HTT$^{-/-}$ rats and wild-type controls (5-HTT$^{+/+}$). We found that baseline functional connectivity values and cocaine-induced neural activity within the corticolimbic network was not significantly altered in 5-HTT$^{-/-}$ versus 5-HTT$^{+/+}$ rats. Similarly, DTI revealed mostly intact white matter structural integrity, except for a reduced fractional anisotropy in the genu of the corpus callosum of 5-HTT$^{-/-}$ rats. At the macroscopic level, analyses of complex graphs constructed from either functional connectivity values or structural DTI-based tractography results revealed that key properties of brain network organization were essentially similar between 5-HTT$^{+/+}$ and 5-HTT$^{-/-}$ rats. The individual tests for differences between 5-HTT$^{+/+}$ and 5-HTT$^{-/-}$ rats were capable of detecting significant effects ranging from 5.8% (fractional anisotropy) to 26.1% (pharmacological MRI) and 29.3% (functional connectivity). Tentatively, lower fractional anisotropy in the genu of the corpus callosum could indicate a reduced capacity for information integration across hemispheres in 5-HTT$^{-/-}$ rats. Overall, the comparison of 5-HTT$^{-/-}$ and wild-type rats suggests mostly limited effects of 5-HTT genotype on MRI-based measures of brain morphology and function.

Introduction

Serotonin (5-HT) is an ancient neurotransmitter that subserves many brain functions, including emotional processing and cognitive flexibility [1,2]. As the serotonin transporter (5-HTT) is a critical modulator of serotonin homeostasis, its dysfunction has been linked to a variety of neuropsychiatric disorders, including anxiety and depression, and substance abuse [3]. A well-known common polymorphism in the promoter region of 5-HTT (5-HTTLPR; 5-HTT-linked polymorphic region) has been studied intensively with regard to anxiety-related traits and vulnerability to depression [4]. More specifically, individuals carrying the low activity (short; s) allelic variant of the 5-HTTLPR show anxiety-like traits and exhibit an increased risk to depression upon stress exposure in early life [5,6]. As these phenotypes have been noted in 5-HTT knockout (5-HTT$^{-/-}$) rodents as well [7], there is strong believe that inherited 5-HTT down-regulation is associated with increased sensitivity to adverse environmental stimuli [8]. Whereas 5-HTT studies are consequently strongly biased to stress effects in 5-HTT genetically compromised individuals, there is also evidence that 5-HTT genotype affects the sensitivity to rewarding environmental stimuli, like drugs of abuse [9]. This was particularly evident in previous studies showing that 5-HTT$^{-/-}$ mice and rats display increased cocaine-induced locomotor activity, cocaine-induced conditioned place preference, and intravenous cocaine self-administration [9–13]. Cocaine is a psychomotor stimulant that acts through inhibition of the serotonin, dopamine and norepinephrine transporter [14]. Whereas the absence of 5-HTT, and thus a failure to increase 5-HT release (JR Homberg, JD Olivier, unpublished observations), may explain the hyperresponsivity to cocaine in 5-HTT$^{-/-}$ rats, there is no clear evidence that such a pharmacological process explains the behavioral response in 5-HTT$^{-/-}$ rats [9]. Alternatively, cocaine may increase mood states [15]. Thereby its intake may serve to alleviate the negative emotional state experienced by 5-HTT$^{-/-}$ rats [16]. As we hypothesized previously, it is possible that developmental increases in 5-HT levels due to reduced 5-HTT availability lead to alterations in the wiring of corticolimbic structures implicated in anxiety-like traits, which are targeted by rewarding environmental stimuli, like cocaine [8]. Structural and functional magnetic resonance imaging (MRI) studies in humans have revealed that 5-HTTLPR s-allele carriers exhibit reduced

perigenual anterior cingulate cortex (pACC) and amygdala volumes, and reduced connectivity between the two [17]. Since the pACC controls emotional responses mediated by the amygdala, it is thought that this decreased cortical control over emotion contributes to the anxiety-like traits in s-allele carriers. This is further corroborated by the observation that blood oxygenation level-dependent (BOLD) responses are increased in the amygdala upon exposure to pictures of fearful faces in functional MRI (fMRI) studies [18]. In 5-HTT$^{-/-}$ rodents, immunohistochemical studies have revealed changes in the dendritic branching and number of spines in amygdala and prefrontal pyramidal neurons [19,20], which may correspond to the structural and functional changes noted in s-allele carriers.

MRI can also be employed in small animal models, which provides a unique opportunity to link rodent and human data. Recent findings from manganese-enhanced MRI of the 5-HTT$^{-/-}$ mouse suggest that there are alterations in reward pathways connecting prefrontal cortex, nucleus accumbens, caudate-putamen, and thalamic nuclei [21]. However, it remains unclear to what extent compromised 5-HTT function in rodents may lead to alterations in basal functional and structural properties of neural network configurations, and whether these properties contribute to cocaine supersensitivity and heightened stress sensitivity in 5-HTT$^{-/-}$ animals. To obtain a comprehensive view of the differences in structural and functional network configurations in 5-HTT$^{-/-}$ rats and wild-type (5-HTT$^{+/+}$) controls, we here applied, for the first time, various MRI paradigms. Brain function in baseline 'resting' condition, and upon cocaine-stimulation, was assessed with resting-state fMRI, and a pharmacological MRI paradigm, respectively. Measures of underlying structural integrity were obtained from Diffusion Tensor Imaging (DTI) using a high-angular resolution diffusion imaging (HARDI) scheme [22]. Finally, we applied various seed-based and voxel-based analyses to explore differences in both local and global functional and structural properties of neural networks between 5-HTT$^{+/+}$ and 5-HTT$^{-/-}$ rats.

Materials and Methods

Ethics statement

All experiments were approved by the Committee for Animal Experiments of the University Medical Center Utrecht, The Netherlands (2007.I.07.098), and all efforts were made to minimize animal suffering and to reduce the number of animals used.

Animals

A total of 31 adult male Wistar rats was used in the study, of which 13 5-HTT$^{+/+}$ (body weight 557.8 $\pm$ 76.5 g) and 18 5-HTT$^{-/-}$ (Slc6a4^{1Hubr}; body weight 492.6 $\pm$ 24.2 g). Experimental animals were derived from crossing heterozygous 5-HTT knock-out rats that were outcrossed for at least ten generations, with wild-type Wistar rats obtained from Harlan Laboratories (The Netherlands). After weaning at the age of 21 days, ear cuts were taken for genotyping, which was performed by Kbiosciences (Hoddesdon, United Kingdom). A 12-h light–dark cycle was maintained, with lights on at 08.00.

Animals were anesthetized with 5% isoflurane (2–2.5% maintenance) in air/O$_2$ (2:1). Two tail veins were cannulated for administration of pancuronium bromide (2 mg/ml) and cocaine HCl dissolved in saline (1 mg/ml), respectively. The left femoral artery was cannulated for blood pressure measurements and blood gas analysis. Three 5-HTT$^{-/-}$ animals were excluded because of complications during surgical preparation. One 5-HTT$^{+/+}$ animal

was excluded from the pharmacological MRI analysis, because of an obstructed intravenous cannula, and because of mechanical ventilation failure two animals (one 5-HTT$^{+/+}$ and one 5-HTT$^{-/-}$) were excluded from the DTI analysis.

MRI acquisition

MRI measurements were conducted on a 4.7T horizontal bore MR system (Varian, Palo Alto, CA), with use of a Helmholtz volume coil (90 mm diameter) and an inductively coupled surface coil (25 mm diameter) for signal excitation and detection, respectively. Rats were mechanically ventilated (CIV 101, Columbus Instruments, Columbus, OH) with 1% end-tidal isoflurane in air/O$_2$ (2:1) and received a continuous infusion of 1 mg/kg/h pancuronium bromide to prevent movement. During MRI, blood oxygen saturation and heart rate were monitored using a pulse oximeter (8600V, Nonin Medical, Plymouth, MN), end-tidal CO$_2$ with a capnograph (Multinex 4200, Datascope Corporation, Paramus, NJ), and mean arterial blood pressure (MABP) from a femoral artery cannulation with a small bore polyethylene tubing connected to a pressure transducer (SA Instruments, Stony Brook, NY). Body temperature was maintained at 37.0 $\pm$ 0.5°C. Before and after resting-state fMRI and pharmacological MRI, arterial CO$_2$ tension (P$_a$CO$_2$) was measured from a sample of 0.15 ml arterial blood (i-STAT, Abbott Laboratories, Princeton, NJ).

First, 10 minutes of resting-state fMRI with high temporal resolution was performed using a T$_2$*-weighted single-shot gradient echo EPI sequence (repetition time (TR)/echo time (TE) = 500/19 ms; 35° flip angle; 64×64 matrix; 0.5×0.5 mm^2 voxels; 7×1.5 mm coronal slices; 1200 BOLD images). Subsequently, gradient-echo multi-slice T$_2$*-weighted pharmacological MRI was performed (TR/TE = 468.75/35 ms; 60° flip angle; 64×64 matrix; 0.5×0.5 mm^2 voxels; 12×1.0 mm coronal slices) with 10 minutes (20 images) of baseline measurements followed by 40 minutes (80 images) acquisition after injection of 1 mg/kg cocaine. Structural connectivity was quantified from a HARDI acquisition scheme that was optimized for whole brain tractography, and also included parameter maps derived from the diffusion tensor, i.e. mean diffusivity and fractional anisotropy. A diffusion-weighted four shot spin-echo EPI sequence (TR/TE = 3500/26 ms; 64×64 matrix; 0.5×0.5 mm^2 voxels; 25×0.5 mm transversal slices; b = 1250 s/mm^2, δ = 6 ms, Δ = 11 ms; 50 diffusion-weighted images in non-collinear directions, and 2 images without diffusion-weighting (b = 0)). Anatomical images for registration purposes were obtained with a 3D gradient-echo sequence (TR/TE = 6/2.576 ms; 40° flip angle; 256×128×128 matrix; field of view = 60×40×40 mm^3; 4 averages).

Image analysis

Using *ANTS* [23], within-subject functional, diffusion-weighted and anatomical images were non-rigidly aligned, and subsequently registered to an anatomical reference image that was matched to a 3D model of a rat brain atlas [24]. All diffusion-weighted, resting-state fMRI, and pharmacological MRI images were corrected for subject motion using *FLIRT* [25]. Resting-state fMRI and pharmacological MRI images were spatially smoothed (Gaussian kernel, full width at half maximum = 1.0 mm), and corrected for linear drift.

After spatial smoothing and intensity scaling, non-neuronal contributions to the resting-state fMRI signal were removed by linear regression, as outlined in [26], with (1) the global mean time-varying signal; (2) six motion correction parameter estimates; (3) a linear trend. Low-frequency fluctuations of the resting-state

BOLD signal were obtained by band-pass filtering between 0.01 and 0.1 Hz.

Analysis of DTI data was performed using *Diffusion Toolkit* [27]. Briefly, data sets were resampled on an isotropic 0.25 mm³ grid, and parameter maps based on voxel-wise estimates of the diffusion tensor were calculated, including fractional anisotropy and mean diffusivity. Whole-brain tractography was obtained from seeds in each voxel according to fractional anisotropy > 0.2 using the interpolated streamline algorithm implementation, with a 35° angle threshold and originating from 10 random seeds in each voxel. Structural connections between any pair of gray matter regions of interest (ROIs; see below) were obtained from tracts that had end points in both ROIs, with a minimum length of 1.0 mm to prevent direct gray matter connections between neighboring areas.

Regions of interest

Bilateral gray matter ROIs that are mainly within the limbic system and receive serotonergic innervations, were projected from the atlas onto the functional time series for seed-based functional connectivity and pharmacological MRI analysis. ROIs included dorsal and ventral medial prefrontal cortices (PFC (dm) and PFC (vm), respectively) [28,29], insula (Ins), frontal cortex (FC), ventral and dorsal orbitofrontal cortices (OFC (v) and OFC (d), respectively), nucleus accumbens (NAc), caudate-putamen (CPu), globus pallidus (GP), basal amygdaloid nuclei (Amy), thalamic nuclei (Tha), dorsal and ventral hippocampus (Hip (d) and Hip (v), respectively), substantia nigra (SN), dorsal raphe nuclei (DRN), ventral tegmental area (VTA), and several cortical areas, i.e. visual (ViC), auditory (AuC), temporal (TeC), parietal (PtC), motor (MC), somatosensory (SmC), and retrosplenial cortex (RsC).

Because of the limited field of view and spatial resolution of the resting-state fMRI data, ROIs that were not reliably identified (i.e., spanning less than two voxels) in at least ten subjects per group, i.e. ventral tegmental area, dorsal raphe nuclei, ventral orbitofrontal cortex, and frontal cortex, were excluded from the resting-state fMRI analyses.

For the analysis of white matter structural integrity from DTI parameter maps, white matter ROIs were first outlined on the mean T_2-weighted $b = 0$ maps. ROIs included the genu and body of the corpus callosum, the anterior part of the anterior commissure, and the anterior part of the internal capsule. An observer - blinded for the animal's genotype - adjusted individual ROIs using each subject's $b = 0$ and fractional anisotropy maps.

Statistical analysis of resting-state fMRI

First, a seed-based analysis of functional connectivity was performed. Functional connectivity was measured as the Fisher z'-transformed correlation coefficient r between pairs of BOLD low-frequency fluctuation signals, i.e. $z' = \ln((1+r)/(1-r))/2$. Functional connectivity values of homologous seeds in the left and right hemisphere were averaged to obtain functional connectivity between pairs of inter-hemispheric and intra-hemispheric ROIs. Functional connectivity was either calculated between two seed regions, or between a seed region's signal and all voxels to obtain functional connectivity maps. One-sample and two-sample *t*-tests determined significant (non-zero) average functional connectivity, and significant differences between groups, respectively. *t*-value maps corresponding to $p < 0.01$ were cluster-corrected ($p < 0.01$, cluster size >160.8 mm³ corresponding to $p < 0.01$, as obtained from Monte Carlo simulations implemented in the *AlphaSim* command available in *AFNI* [30,31]).

Second, to obtain a comprehensive, quantitative view of the complex interactions among brain regions in terms of their functional couplings, we applied a graph theory perspective to analyze global properties of complex functional brain networks [32–35]. For each subject, a weighted undirected graph $G = (V, W)$ was constructed (*R* software; *igraph* package [36]), with a collection of nodes V and a collection of edge weights W. A node represented a ROI with an associated mean time-varying signal. Edges between each pair of nodes were weighted by the correlation coefficient between their signals. Whereas analysis of binary graphs requires an arbitrary threshold to separate strong from weak edge connections, we computed measures that utilize all edges in a weighted manner, except for edges that have negative weights or represent self-connections [34]. From these graphs we calculated global measures of (1) segregated/modular information processing, i.e. the clustering coefficient (average of local clustering coefficients) [37]; (2) integrated/distributed information processing, i.e. the characteristic path length (average of all shortest path lengths) [38]; and (3) the balance between global and local efficiency of parallel information processing, i.e., 'small-worldness' [39,40]. Clustering coefficients and characteristic path lengths were normalized based on 1000 instances of surrogate random networks obtained through random edge weights permutations for each subject's graph [41]. When appropriate, effect sizes (Cohen's *d*) and corresponding *t*-values are reported.

Statistical analysis of pharmacological MRI

The pharmacological MRI data was analyzed in three different ways: (1) to test whether the BOLD time course after i.v. cocaine injection was different between 5-HTT$^{+/+}$ and 5-HTT$^{-/-}$ animals on a seed-by-seed basis; (2) to assess differences in the peak activation and total activation following cocaine, using a seed-by-seed parametric fit; and (3) to obtain voxel-level maps of group-level neural activity, and differences in the BOLD response, upon cocaine stimulation.

First, we tested on a seed-by-seed basis whether the BOLD response after i.v. cocaine injection was different between the two groups. For each ROI, we tested the mean preprocessed time series data between the groups in a generalized least squares fit (*R* software; *nlme* package [42]). To account for autocorrelation in the BOLD measurements we included a continuous-time first-order autoregressive error term AR(1). Group and time were taken as main effects, and as covariates the P_aCO_2 before pharmacological MRI, and the MABP before, and at peak response (between 5 and 15 minutes) after cocaine injection, i.e. %BOLD ~ group + time + $P_aCO_{2\ before}$ + MABP$_{before}$ + MABP$_{peak}$. Means and standard errors of the group effect were estimated using normalized response and predictor variables.

Second, we fitted a three-parameter function f dependent on time t after cocaine injection, from which we could easily calculate total activation (i.e., area under the curve), and peak activation. Here, $f_{\alpha,\beta,\lambda}(t) = \lambda g_{\alpha,\beta}(t)$ with shape (α) and rate (β) parameters of a gamma-variate function, $g_{\alpha,\beta}(t) = \Gamma^{-1}(\alpha)\beta^\alpha x^{\alpha-1}e^{-\beta t}$, multiplied by a scale factor (λ). Fitting was performed in a Bayesian framework using Markov Chain Monte Carlo (MCMC) methods as implemented in *JAGS* [43] and interfaced from *R* (*R2jags* package), to obtain for each subject and ROI a parametric estimate of the signal change relative to the baseline value. In a hierarchical design, group-level distributions structured the between-subject variation in model parameters. Such hierarchical models provide constraints to the fits of individual time courses, thus improving the parameter estimates at the individual ROI level in the presence of noise, and are easily specified in a Bayesian setting. A caveat of this design is that suitable priors need to be specified to obtain robust fits. We have therefore defined prior distribution parameters based on model parameters of initial

subject-level fits. From the subject-level model parameter estimates we calculated maximum signal change, and total activation (area under curve). To test for an overall group difference, a linear mixed-model analysis was performed (R software; $nlme$ package [42]) separately for maximum signal change and area under the curve, taking group and time as fixed main effects, P_aCO_2 $_{before}$, MABP $_{before}$, and MABP $_{peak}$ as covariates, and the ROIs per subject as random effects.

Third, we obtained group-level spatial maps of BOLD activation upon cocaine stimulation using a voxel-based generalized least squares fit, with an AR(1) correlation structure to account for autocorrelation in the time series data, for a design matrix that was constructed according to the procedure described in [44]. Briefly, the design matrix consisted of (1) a representative gamma-variate response curve; (2) the frame-by-frame motion correction parameters (six degrees of freedom); (3) the first three components of a singular value decomposition of variations in evolution of the BOLD response as modeled in (1). Each subject was fitted separately, and the estimates of the coefficients of the response function (1) were then analyzed for group differences using a linear model fit, with as covariates the P_aCO_2 $_{before}$, and the pre- and post-injection MABP levels, i.e. MABP $_{before}$ and MABP $_{peak}$. t-value maps corresponding to $p < 0.05$ were cluster-corrected (cluster size >12.0 mm^3 corresponding to $p < 0.05$, as obtained from Monte Carlo simulations implemented in the $AlphaSim$ command available in AFNI [30,31]).

In all generalized least squares, linear model, and linear mixed-model fits, missing covariate values were replaced by their group mean values [45].

Statistical analysis of DTI

First, in a tract-based spatial statistics (TBSS) approach as implemented in FSL [46], voxel-wise analysis of white matter structural integrity was performed after projecting fractional anisotropy values onto a common white matter skeleton, to account for residual alignment inaccuracies after non-rigid inter-subject registration and to limited the number of tests.

Second, a seed-based analysis of differences in white matter fractional anisotropy values was performed for the four manually outlined ROIs. Gray matter differences in fractional anisotropy were tested for the ROIs projected from the stereotaxic atlas.

Third, analogous to the complex functional brain networks constructed from the resting-state fMRI functional connectivity values, we constructed from the DTI-based fiber tracts for each subject a complex graph expressing structural connectivity among the 23 bilaterally positioned cortical and subcortical gray matter ROIs. The edges between the regions were weighted by the mean fractional anisotropy along the connecting tracts. As described above, we calculated from these graphs the normalized clustering coefficient and normalized characteristic path length, and small-worldness as the ratio between the two former measures.

Results

Resting-state functional MRI

Figure 1 depicts overall significantly non-zero (false discovery rate (FDR)-adjusted $p < 0.05$, one-sample t-test) functional connectivity values among the seed ROIs across all 5-HTT$^{+/+}$ and 5-HTT$^{-/-}$ animals, color-coded with the corresponding z-value. To increase the statistical power of between-group t-tests and obtain functional connectivity between pairs of inter-hemispheric and intra-hemispheric ROIs, functional connectivity values of homologous seeds in the left and right hemisphere were averaged. Strong inter-hemispheric functional connectivity be-

tween homologous ROIs was observed for almost all seeds. To assess whether group-level functional connectivity values differed between the 5-HTT$^{+/+}$ and 5-HTT$^{-/-}$ groups, we performed pairwise two-sample t-tests (Figure 1, bottom row). Differences in functional connectivity between 5-HTT$^{+/+}$ and 5-HTT$^{-/-}$ rats were not significant after FDR-correction for multiple comparisons. Uncorrected p-values ($p < 0.05$) show differences between 5-HTT$^{+/+}$ and 5-HTT$^{-/-}$ rats in intra-hemispheric functional connectivity between dorsal hippocampus and auditory cortex ($t(20) = 2.4$; effect size: Cohen's $d = 1.07$), caudate-putamen ($t(24) = -2.1$; $d = -0.87$) and dorsal orbitofrontal cortex ($t(13) = -3.0$; $d = -1.65$), between somatosensory cortex and insula ($t(24) = 2.2$; $d = 0.89$), and between visual cortex and somatosensory cortex ($t(18) = 2.3$; $d = 1.06$) and ventromedial prefrontal cortex ($t(22) = -2.4$; $d = -1.02$). Inter-hemispheric functional connectivity was significantly different ($p < 0.05$, uncorrected) between dorsomedial prefrontal cortex and amygdala, ($t(24) = -2.1$; $d = -0.87$); between caudate-putamen and nucleus accumbens ($t(24) = -2.5$; $d = -1.02$) and substantia nigra ($t(20) = -2.2$; $d = -0.99$); between temporal cortex and insula ($t(18) = -2.2$; $d = -1.03$) and retrosplenial cortex ($t(18) = -2.2$; $d = -1.05$); and between visual cortex and insula ($t(21) = -2.5$; $d = -1.07$) and ventromedial prefrontal cortex ($t(22) = -2.5$; $d = -1.06$).

Figure 2 shows functional connectivity maps (seed-based, only significant non-zero functional connectivity after cluster-correction) with seeds in ventromedial prefrontal cortex, thalamus, and caudate-putamen, for both groups. Ventromedial prefrontal cortex displayed significant positive functional connectivity with retrosplenial cortex, and thalamic nuclei. On the other hand, thalamic nuclei showed negative functional connectivity values with caudate-putamen, nucleus accumbens, and cortical somatosensory areas.

The functional brain networks constructed from seed-based resting-state fMRI functional connectivity values were characterized by the normalized clustering coefficient, the normalized characteristic path length, and the ratio between these two values, i.e., small-worldness (Figure 3). We found that both characteristic path length and clustering coefficient were larger than observed in random networks, and the networks exhibited 'small-world' properties, i.e. the ratio between normalized clustering coefficient and normalized characteristic path length was slightly larger than 1, indicating a more clustered organization while maintaining relatively low shortest path lengths. The normalized clustering coefficient was found to be 1.50 ± 0.12 in 5-HTT$^{+/+}$ and 1.55 ± 0.15 in 5-HTT$^{-/-}$ ($d = -1.50$), the normalized characteristic path length 1.34 ± 0.09 in 5-HTT$^{+/+}$ and 1.36 ± 0.10 in 5-HTT$^{-/-}$ ($d = -0.73$), and small-worldness 1.12 ± 0.04 in 5-HTT$^{+/+}$ and 1.14 ± 0.06 in 5-HTT$^{-/-}$ ($d = -1.81$). We found no significant differences in these global resting-state fMRI functional connectivity graph parameters between wild-types and knockouts.

Pharmacological MRI

Before MRI, ventilation volume was determined by body weight, and subsequent adjustments were aimed at maintaining normal P_aCO_2 levels. To account for within- and between-group variations in baseline P_aCO_2, and variations in blood pressure before and after cocaine injection, these values were included as covariates in the statistical analyses. Baseline P_aCO_2 was 39.2 ± 2.5 mmHg in 5-HTT$^{+/+}$ and 34.7 ± 7.3 mmHg in 5-HTT$^{-/-}$. MABP went from 118.2 ± 41.8 mmHg (baseline) to 117.1 ± 39.2 mmHg (between 5 and 15 minutes after cocaine injection) in 5-HTT$^{+/+}$, and from 126.8 ± 26.3 mmHg to 129.2 ± 25.7 mmHg in 5-HTT$^{-/-}$.
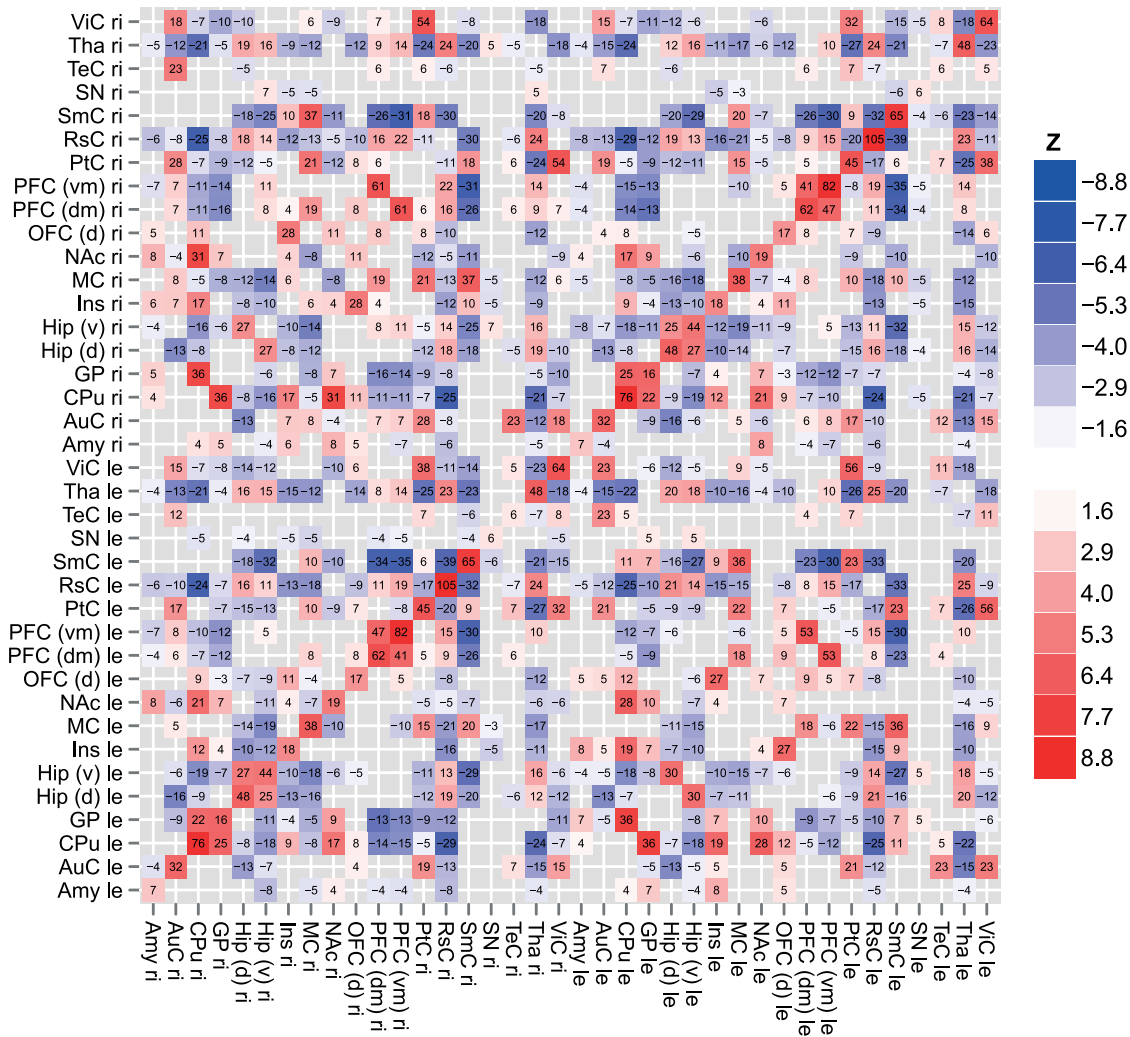
Figure 1. Seed-based resting-state fMRI functional connectivity matrices. Resting-state fMRI-based functional connectivity values were calculated and tested for significance ($p < 0.05$, one-sample t-test) across all 5-HTT^{+/+} and 5-HTT^{-/-} animals, among all seed regions in left (le) and right (ri) hemispheres. Significant non-zero functional connectivity values were scaled by 10^2 and color-coded according to Z, the normalized t-value. The p-values were false discovery rate (FDR) adjusted for multiple comparisons. *Amy*: basal amygdaloid nuclei; *AuC*: auditory cortex; *CPu*: caudate-putamen; *GP*: globus pallidus; *Hip (d)*: dorsal hippocampus; *Hip (v)*: ventral hippocampus; *Ins*: insula; *MC*: motor cortex; *NAc*: nucleus accumbens; *OFC (d)*: dorsal orbitofrontal cortex; *PFC (dm)*: dorsomedial prefrontal cortex; *PFC (vm)*: ventromedial prefrontal cortex; *PtC*: parietal cortex; *RsC*: retrosplenial cortex; *SmC*: somatosensory cortex; *SN*: substantia nigra; *TeC*: temporal cortex; *Tha*: thalamic nuclei; *ViC*: visual cortex.
doi:10.1371/journal.pone.0057780.g001

On average, the 5-HTT^{-/-} animals displayed a slightly higher pharmacological MRI profile following intravenous cocaine injection (Figure 4A). To test whether the group-mean responses were statistically different when accounting for confounding effects of physiological status on the BOLD response, we applied a generalized least squares fit with a correction for temporal autocorrelation, and included P_aCO_2 and MABP measures as covariates. We found significant ($p < 0.05$, uncorrected) group differences with a seed-based generalized least squares fit in the basal amygdaloid nuclei, dorsal raphe nuclei, frontal cortex, substantia nigra, temporal cortex, and visual cortex (Table 1). However, following correction for multiple comparisons, the FDR-adjusted p-values were all larger than 0.05.

Using a hierarchical Bayesian approach, we fitted a three-parameter gamma-variate function on the average time signal in each ROI, for each subject separately. From the fits we calculated the estimated peak amplitude (maximum relative BOLD re-

sponse), as well as the area under the curve. Linear mixed-model analyses found no significant overall differences between the two groups for maximum response and area under the curve. We tested also with a generalized least squares regression for differences between the groups separately for each region of interest (Table 2). Differences for the area under the curve in the retrosplenial cortex, somatosensory cortex, and visual cortex (Figure 4B, Table 2) were only significant ($p < 0.05$) without correction for multiple comparisons.

MCMC-sampled differences (5-HTT^{+/+} − 5-HTT^{-/-}) between estimates of the group mean of gamma-variate function parameters were not significantly different from zero, i.e. with zero contained in the 95% credible interval ($_{95\%}$CI) around the mean, for shape (mean 0.20, $_{95\%}$CI = [-0.02, 0.42]), rate (mean 0.008, $_{95\%}$CI = [-0.010, 0.024]), and scale factor (mean -2.8, $_{95\%}$CI = [-11.3, 5.0]).
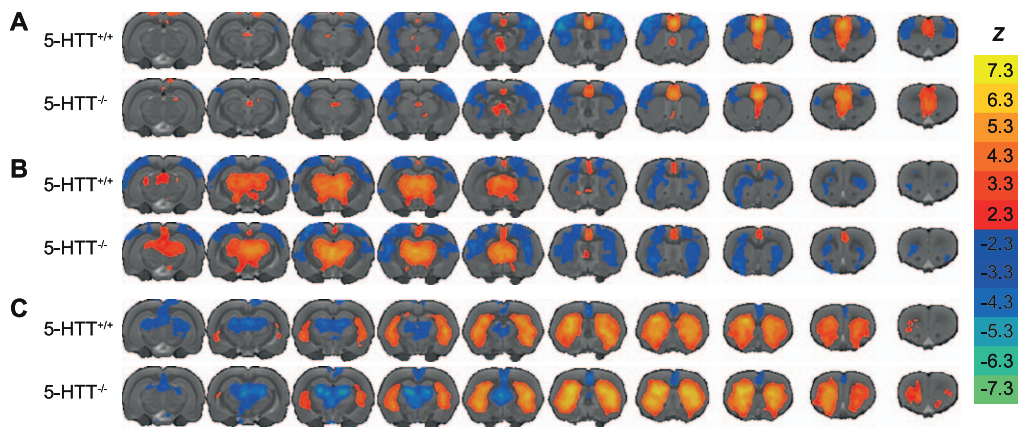
Figure 2. Maps of seed-based resting-state fMRI functional connectivities. The resting-state fMRI signal of a seed region was correlated with all voxels in the brain. For each voxel, a one-sample t-test was performed to determine whether the signal at that location correlated significantly with the seed-region. Group-level resting-state fMRI-based functional connectivity maps are displayed for three different seed regions. Voxels that exhibit significant ($p < 0.01$, cluster-corrected) functional connectivity with a seed region in (A) ventromedial prefrontal cortex, (B) thalamic nuclei, and (C) caudate-putamen, are color-coded according to Z-value thresholded at 2.3 ($p < 0.01$) for both positive (red to yellow) and negative (blue to light blue) correlations between the filtered time-varying signals, and overlaid on a multi-slice anatomical rat brain template.
doi:10.1371/journal.pone.0057780.g002

In a voxel-based analysis we observed widespread cocaine-induced activation in large parts of the cerebral cortex, as well as in hippocampus, dorsal and ventral striatum, and thalamic nuclei. Group mean response maps were calculated from a voxel-wise one-sample t-test (Figure 5). The cerebral pharmacological MRI response was found to be positive everywhere, and highly similar between wild-type and knockout rats. No significant differences between the two groups were found from a voxel-by-voxel fit.
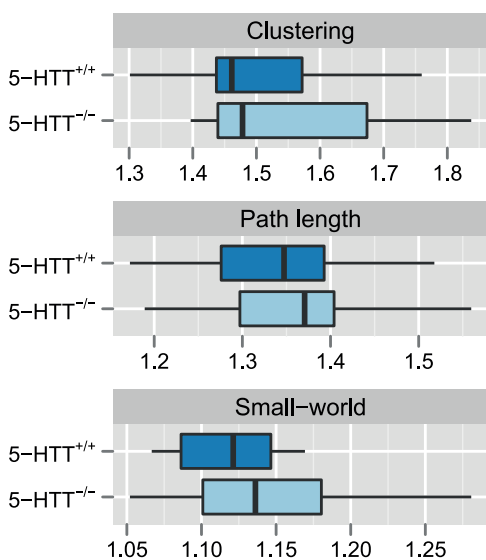

Figure 3. Network parameters from seed-based graph analysis of resting-state fMRI functional connectivity. Functional brain networks were constructed from seed-based resting-state fMRI functional connectivity values. The boxplots display three global network parameters that capture key properties of the functional brain networks, and were calculated on weighted graphs: the clustering coefficient (i.e., average of local clustering coefficients), the characteristic path length (i.e., average of shortest path lengths), and the small-worldness (i.e., ratio of normalized clustering coefficient and normalized characteristic path length).
doi:10.1371/journal.pone.0057780.g003

Diffusion tensor imaging

At the voxel level, we found no evidence for differences in white matter integrity, as expressed by DTI fractional anisotropy values, between 5-HTT$^{+/+}$ and 5-HTT$^{-/-}$, using the TBSS approach. However, two-sample t-test showed that there was a significantly lower fractional anisotropy in the genu of the corpus callosum of 5-HTT$^{-/-}$ animals as compared to wild-types ($t = $ -3.33; FDR-adjusted $p < 0.05$; effect size, Cohen's $d = $ -1.31) (Figure 6). We did not find statistically significant differences in the other three white matter ROIs (anterior commissure: $d = $ 0.35; body of the corpus callosum: $d = $ -0.31; internal capsule: $d = $ -0.08). Differences in fractional anisotropy and mean diffusivity in gray matter regions also did not reach statistical significance (data not shown).

Similar to the functional brain network analysis, we obtained structural brain networks constructed from whole-brain DTI-based tractography and weighted by the average fractional anisotropy value along the connecting tracts. The normalized clustering coefficient was found to be 1.74 ± 0.19 in 5-HTT$^{+/+}$ and 1.68 ± 0.13 in 5-HTT$^{-/-}$ (effect size, Cohen's $d = $ -1.36), the normalized characteristic path length 1.10 ± 0.03 in 5-HTT$^{+/+}$ and 1.09 ± 0.05 in 5-HTT$^{-/-}$ ($d = $ -0.90), and small-worldness 1.59 ± 0.18 in 5-HTT$^{+/+}$ and 1.55 ± 0.12 in 5-HTT$^{-/-}$ ($d = $ -0.96) (Figure 7). Again, the ratio between normalized clustering coefficient and normalized characteristic path length indicated that the structural brain networks exhibit small-world characteristics. However, we found no significant differences in these global tractography-based graph parameters between wild-types and knockouts.

Discussion

The 5-HTT$^{-/-}$ phenotype has been associated with cocaine hyperresponsivity [10], increased stress sensitivity [7] and anxiety- and depression-like behavior [16] in rats. As reduced functional 5-HTT expression and subsequent increases in 5-HT levels may affect normal development of interconnections among corticolimbic structures implicated in anxiety-like traits [8], we applied various MRI paradigms to assess the effect of 5-HTT$^{-/-}$ rat genotype on the functional and structural properties of neural

Table 1. Cocaine-induced brain activation: results from seed-based generalized least squares fit of pharmacological MRI response.

Region	Coefficient ± SE	t-value	p-value	d
Dorsal hippocampus	$-5.71 \times 10^{-2} \pm 9.19 \times 10^{-2}$	−0.62	0.535	−0.03
Auditory cortex	$-2.56 \times 10^{-1} \pm 1.35 \times 10^{-1}$	−1.90	0.057	−0.08
Basal amygdaloid nuclei	$1.22 \times 10^{-1} \pm 5.7 \times 10^{-2}$	2.13	0.033*	0.09
Caudate-putamen	$-4.56 \times 10^{-2} \pm 9.84 \times 10^{-2}$	−0.46	0.643	−0.02
Dorsomedial prefrontal cortex	$-2.18 \times 10^{-1} \pm 1.54 \times 10^{-1}$	−1.42	0.156	−0.06
Dorsal orbitofrontal cortex	$-8.15 \times 10^{-3} \pm 1.63 \times 10^{-1}$	−0.05	0.960	−0.00
Dorsal raphe nuclei	$-1.96 \times 10^{-1} \pm 7.92 \times 10^{-2}$	−2.47	0.014*	−0.12
Frontal cortex	$-2.33 \times 10^{-1} \pm 1.13 \times 10^{-1}$	−2.06	0.040*	−0.09
Globus pallidus	$-5.12 \times 10^{-3} \pm 3.94 \times 10^{-2}$	−0.13	0.897	−0.01
Insula	$-5.61 \times 10^{-2} \pm 1.5 \times 10^{-1}$	−0.38	0.708	−0.02
Motor cortex	$-1.46 \times 10^{-1} \pm 1.62 \times 10^{-1}$	−0.90	0.366	−0.04
Nucleus accumbens	$-3.77 \times 10^{-2} \pm 9.31 \times 10^{-2}$	−0.41	0.685	−0.02
Parietal cortex	$-9.71 \times 10^{-2} \pm 1.59 \times 10^{-1}$	−0.61	0.542	−0.03
Ventral hippocampus	$-1.3 \times 10^{-1} \pm 9.03 \times 10^{-2}$	−1.44	0.150	−0.06
Retrosplenial cortex	$-1.97 \times 10^{-1} \pm 1.57 \times 10^{-1}$	−1.26	0.208	−0.05
Substantia nigra	$-3.11 \times 10^{-1} \pm 1.03 \times 10^{-1}$	−3.02	0.003**	−0.13
Somatosensory cortex	$-1.11 \times 10^{-2} \pm 1.71 \times 10^{-1}$	−0.07	0.948	−0.00
Temporal cortex	$-4.34 \times 10^{-1} \pm 9.38 \times 10^{-2}$	−4.63	0.000**	−0.20
Thalamic nuclei	$-2.02 \times 10^{-1} \pm 1.24 \times 10^{-1}$	−1.63	0.104	−0.07
Visual cortex	$-3.47 \times 10^{-1} \pm 1.67 \times 10^{-1}$	−2.08	0.037*	−0.09
Ventromedial prefrontal cortex	$8.72 \times 10^{-2} \pm 1.71 \times 10^{-1}$	0.51	0.610	0.02

Coefficients, standard error (SE), t-value, p-value, and effect size (Cohen's d), for generalized least squares analysis of differences in the pharmacological MRI response between 5-HTT$^{+/+}$ and 5-HTT$^{-/-}$ rats. Response and predictor variables were normalized. *$p < 0.05$, **$p < 0.005$, uncorrected.
doi:10.1371/journal.pone.0057780.t001

networks under baseline conditions, and upon a rewarding cocaine stimulus. We observed typical functional connectivity patterns and robust hemodynamic responses following an intravenous cocaine injection, but our results do not suggest major alterations in baseline functional connectivity and cocaine-induced neural activity within the corticolimbic network. Similarly, white matter structural integrity seems largely unaffected by the lack of 5-HTT expression, except for the genu of the corpus callosum. At the macroscopic level, tractography-based graph analysis revealed that key properties of brain network organization were essentially similar between 5-HTT$^{-/-}$ and 5-HTT$^{+/+}$ rats.

The distinctive patterns of positive and negative functional connectivity, as displayed in seed-based resting-state fMRI functional connectivity maps, suggest broad segregation of functional networks. For instance, resting-state activity in the thalamic nuclei mostly correlated with that in retrosplenial and medial prefrontal regions, but not with that in caudate-putamen and somatosensory areas. However, cautious interpretation of negative and near-zero correlation values is warranted, as these may partly be the by-product of removing the global mean signal during pre-processing [26].

In 5-HTT$^{-/-}$ mice, increased stress- and depression-like [19,47] and abnormal anxiety-related behavior [48,49] have been associated with morphological changes in ventromedial prefrontal cortex and basolateral amygdala [19], potentially contributing to changes in corticolimbic function. Spatiotemporal differences in neuronal tracer accumulation measured with manganese-enhanced MRI provided evidence for developmental alterations in the reward circuitry of 5-HTT$^{-/-}$ mice, in the absence of significant differences in brain metabolite levels, gray matter morphology,

and white matter integrity [21]. Here, we did not find significant differences between 5-HTT$^{+/+}$ and 5-HTT$^{-/-}$ rats with regard to resting-state fMRI functional connectivity values between specific ROIs, after correction for multiple comparisons. Furthermore, comparisons of functional neural networks using complex graph analysis parameters did not reveal major differences in key organizational properties between wild-types and knockouts. However, resting-state fMRI and manganese-enhanced MRI provide qualitatively different views of functional connections among the brain regions involved in reward processing. Whereas the former measures the instantaneous synchronicity of spontaneous neuronal signaling, the latter highlights direct anatomical pathways between neuronal populations. Although the uptake and trans-synaptic transfer of manganese is greatly facilitated by voltage-gated calcium channels [50,51], anterograde axonal transport is not necessarily activity-dependent [52,53]. The neural tracts thus traced provide an integrative measure of local structural connectivity and relative neuronal activity during the period after tracer injection. While resting-state fMRI-based functional connectivity is largely associated with direct structural connectivity (e.g., as measured with DTI), synchronization through indirect synaptic connections also contributes to the observed functional connectivity [54,55]. Manganese-enhanced MRI of 5-HTT$^{-/-}$ mice identified that the balance between mesolimbic, mesocortical, and nigrostriatal connections and activity was shifted towards the latter two pathways [21]. Our resting-state fMRI analysis did not reveal a difference in functional connectivity among the regions involved in these pathways, suggesting that the alterations in reward circuitry are not explained by changes in oscillatory coupling between these regions.
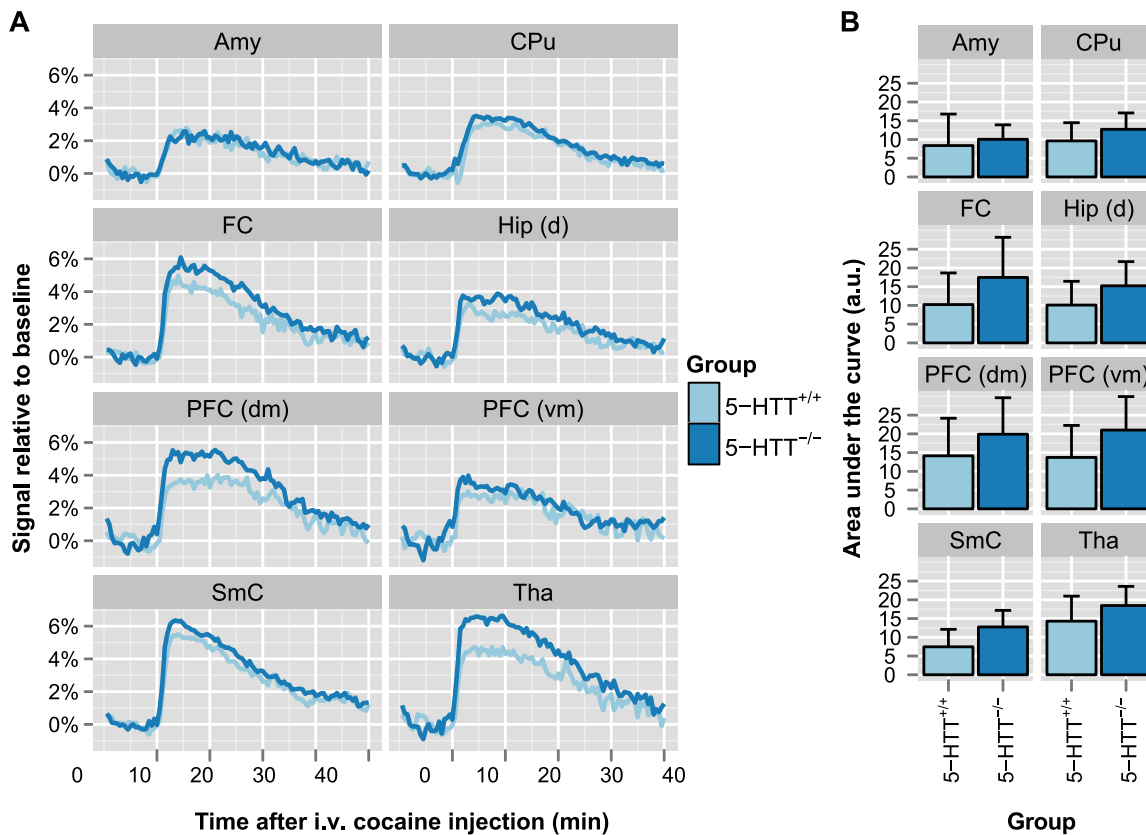
Figure 4. Cocaine-induced activation responses from seed-based analysis of pharmacological MRI. BOLD-based pharmacological MRI was performed for 50 minutes, with 1 mg/kg cocaine injected intravenously after 10 minutes. (A) The raw signal time-courses after preprocessing, and (B) the area-under-the curve of gamma-variate functions obtained with a Bayesian fitting routine, are displayed for a selection of seed regions. *Amy*: basal amygdaloid nuclei; *CPu*: caudate-putamen; *FC*: frontal cortex; *Hip (d)*: dorsal hippocampus; *PFC (dm)*: dorsomedial prefrontal cortex; *PFC (vm)*: ventromedial prefrontal cortex; *SmC*: somatosensory cortex; *Tha*: thalamic nuclei.
doi:10.1371/journal.pone.0057780.g004

In human s-allele carriers, increased fMRI activation upon fearful stimuli [56,57], and increased functional coupling between ventromedial prefrontal cortex and amygdala, possibly limiting the capacity to control emotional states under stressful conditions [58], has been explained by a reduced amygdala activation in the neutral versus fixation condition [59]. Resting-state quantitative EEG measurements linked low 5-HTT expression to overall lower spectral powers [60], and higher resting-state cerebral blood flow in amygdala and hippocampus, further supporting the hypothesis that 5-HTT genotype modulates resting activity rather than stimulus-induced activation [61]. In contrast, a recent study that addressed earlier reports of resting-state cerebral blood flow modulation in amygdala and ventromedial prefrontal cortex by 5-HTTLPR [62], concluded from a larger cohort that there was no association between 5-HTT genotype and baseline brain perfusion [63]. This is in agreement with our results, which indicate that baseline neural network configurations as measured with resting-state fMRI functional connectivity are generally independent of 5-HTT genotype.

5-HTT genotype has been associated with increased sensitivity to rewarding environmental stimuli like drugs of abuse, e.g. with s-allele carriers exhibiting increased alcohol use [64,65] and drug dependence [65], and increased risk for developing cocaine use mediated by early environmental factors [66]. Similarly, 5-HTT$^{-/-}$ mice and rats display increased cocaine-induced locomotor activity, cocaine-induced conditioned place preference, and

intravenous cocaine self-administration [9–13]. On average, we found that 5-HTT$^{-/-}$ rats displayed a slightly higher pharmacological MRI profile following intravenous cocaine, but after accounting for confounding differences in physiological status, and correcting for multiple statistical comparisons, the hemodynamic responses did not reflect the increased responsivity to cocaine as established in 5-HTT$^{-/-}$ rats at the behavioral level [9,10]. One important difference with human fMRI studies, and previous behavioral assessments in rats, is the necessary application of general anesthesia during pharmacological MRI. While cocaine inhibits ligand binding at the dopamine, serotonin and norepinephrine transporters [67], isoflurane further increases striatal dopamine levels [68] by reducing functional dopamine transporter availability [69]. Volatile anesthetics modulate serotonergic neurotransmission as well, with isoflurane decreasing extracellular 5-HT in mouse hippocampus [70] despite reduced synaptosomal uptake of 5-HT *in vitro* [71]. However, a stronger reduction of hippocampal 5-HT reuptake in 5-HTT$^{-/-}$ as compared to 5-HTT$^{+/+}$ mice [70] suggests that 5-HTT is not a major target of isoflurane *in vivo* in the present study. Furthermore, it has been shown that isoflurane and alpha-chloralose differentially affect baseline cerebral blood flow [72] and cocaine-induced hemodynamic and pharmacokinetic responses [73]. Although in the current study animals were minimally anesthetized with 1.0% isoflurane, drug-anesthetic interaction effects on cerebral hemodynamics and neurotransmitter function might in part explain

Table 2. Cocaine-induced brain activation: results from Bayesian fit of gamma-variate function to pharmacological MRI data.

	Maximum of the BOLD response, relative to baseline (%)				Area under the curve (a.u.)			
Region	5-HTT^{+/+}	5-HTT^{-/-}	t	d	5-HTT^{+/+}	5-HTT^{-/-}	t	d
Dorsal hippocampus	3.3 ± 1.7	4.5 ± 2.0	0.85	0.33	10.1 ± 6.3	15.2 ± 6.5	1.09	0.42
Auditory cortex	8.3 ± 5.1	9.2 ± 3.3	0.02	0.01	18.5 ± 8.4	23.9 ± 7.2	1.15	0.45
Basal amygdaloid nuclei	2.8 ± 1.9	3.1 ± 1.2	−0.23	−0.09	8.4 ± 8.4	10.0 ± 3.9	−0.13	−0.05
Caudate-putamen	3.2 ± 1.6	3.8 ± 1.3	0.56	0.22	9.6 ± 4.9	12.7 ± 4.4	0.91	0.35
Dorsomedial prefrontal cortex	4.6 ± 2.9	6.0 ± 2.6	1.02	0.39	14.1 ± 10.0	19.9 ± 9.7	0.99	0.38
Dorsal orbitofrontal cortex	4.6 ± 2.9	3.8 ± 2.8	−0.65	−0.25	14.0 ± 9.5	12.3 ± 9.7	−0.52	−0.20
Frontal cortex	4.1 ± 3.6	6.1 ± 3.4	0.20	0.08	10.2 ± 8.4	17.5 ± 10.7	0.74	0.29
Globus pallidus	5.6 ± 2.8	5.2 ± 2.1	0.02	0.01	16.1 ± 8.2	16.0 ± 6.6	0.16	0.06
Insula	2.8 ± 1.8	3.7 ± 1.2	0.62	0.24	7.8 ± 5.7	10.8 ± 3.7	0.54	0.21
Motor cortex	4.6 ± 2.3	5.8 ± 1.8	0.93	0.36	13.6 ± 6.9	18.6 ± 6.1	1.27	0.49
Nucleus accumbens	4.6 ± 2.2	5.7 ± 1.7	1.23	0.48	13.4 ± 6.3	18.6 ± 4.9	1.82	0.71
Parietal cortex	2.5 ± 1.5	2.4 ± 1.9	−1.10	−0.43	6.2 ± 3.6	7.7 ± 6.5	−0.15	−0.06
Ventral hippocampus	7.2 ± 3.7	7.5 ± 2.7	−0.24	−0.09	18.0 ± 8.6	22.0 ± 7.5	0.53	0.20
Retrosplenial cortex	2.6 ± 1.5	4.0 ± 1.6	1.57	0.61	7.4 ± 4.6	12.9 ± 4.7	2.10*	0.81
Substantia nigra	5.0 ± 3.3	6.5 ± 2.1	0.79	0.31	11.9 ± 7.4	19.4 ± 7.5	1.65	0.64
Somatosensory cortex	3.1 ± 1.5	4.2 ± 1.4	1.17	0.45	7.5 ± 4.7	12.8 ± 4.4	2.22*	0.86
Thalamic nuclei	5.1 ± 2.4	6.1 ± 2.0	0.64	0.25	14.3 ± 6.7	18.5 ± 5.1	1.02	0.40
Visual cortex	5.0 ± 2.8	7.5 ± 2.7	1.63	0.63	12.8 ± 6.2	22.1 ± 7.2	2.56*	0.99
Ventromedial prefrontal cortex	4.5 ± 2.3	6.6 ± 2.9	1.20	0.46	13.7 ± 8.5	21.0 ± 8.9	1.14	0.44

Group-wise mean ± standard deviation, t-value from two-sample t-test, and effect size (Cohen's d), for two parameters calculated from Bayesian fits of a gamma-variate function to the pharmacological MRI response after intravenous cocaine injection. *$p < 0.05$, uncorrected.
doi:10.1371/journal.pone.0057780.t002

differences between observations in awake and anesthetized animals, and potentially obscure the effects of 5-HTT genotype on BOLD-based measures of neural activity.

The potential effects of developmental alterations in 5-HT homeostasis are not limited to gray matter. It has been shown that axonal uptake of 5-HT is reduced by selective inhibition of 5-HTT [74]. Furthermore, the importance of early-life 5-HT homeostasis has been demonstrated by transient inhibition of 5-HTT function with selective serotonin reuptake inhibitors, which altered cortical network function, callosal axon myelination, and oligodendrocyte soma morphology in rat pups after perinatal citalopram treatment [75], while early postnatal fluoxetine treatment in mice produced similar deficits in emotional behavior as observed in 5-HTT knockouts [76]. Our seed-based DTI-analysis highlights a small
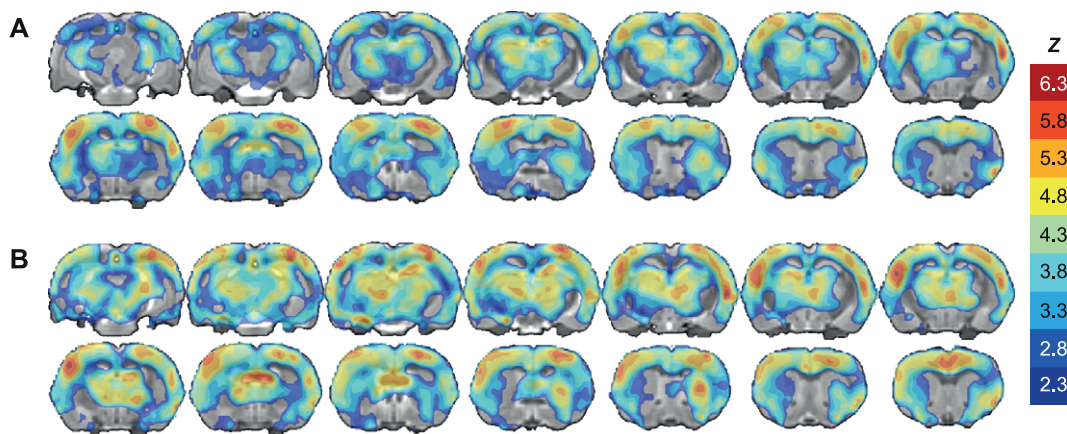

Figure 5. Cocaine-induced activation pattern from voxel-based analysis of pharmacological MRI. BOLD-based pharmacological MRI was performed for 50 minutes, with 1 mg/kg cocaine injected intravenously after 10 minutes. The maps display the group-level results from a voxel-based analysis of cocaine-induced brain activation, obtained from second-level analysis of subject-level generalized least squares fits of the pharmacological MRI signals in (A) 5-HTT^{+/+}, and (B) 5-HTT^{-/-} animals. The maps display Z-values of significantly activated voxels ($p < 0.01$, cluster-corrected). Positive responses are color-coded between $Z = [2.3, 6.3]$, and overlaid on a multi-slice anatomical rat brain template.
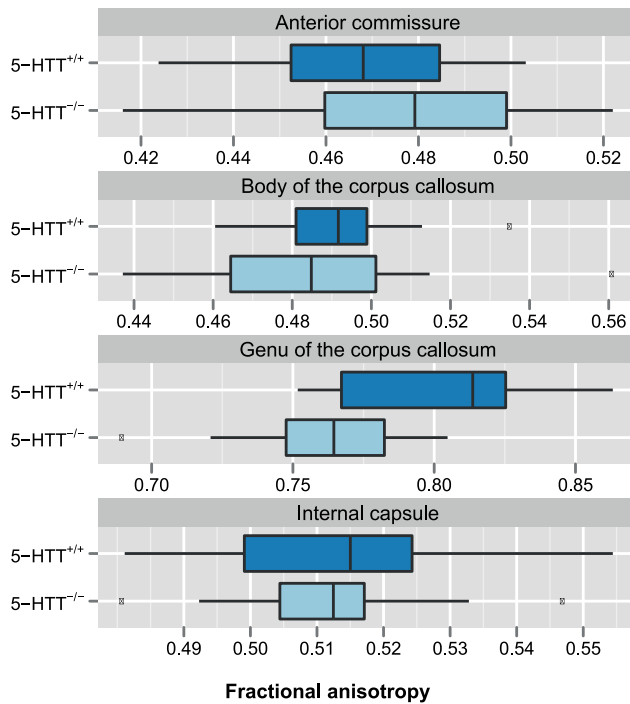doi:10.1371/journal.pone.0057780.g005

Figure 6. White matter fractional anisotropy values from seed-based analysis of fractional anisotropy maps. DTI fractional anisotropy was measured in four different white matter seed regions. Boxplots display for 5-HTT$^{-/-}$ and 5-HTT$^{+/+}$ animals the average value in each of the regions. Fractional anisotropy was significantly lower in the genu of the corpus callosum of 5-HTT$^{-/-}$ animals (two-sample t-test, $t =$ -3.33, false discovery rate (FDR)-adjusted $p < 0.05$).
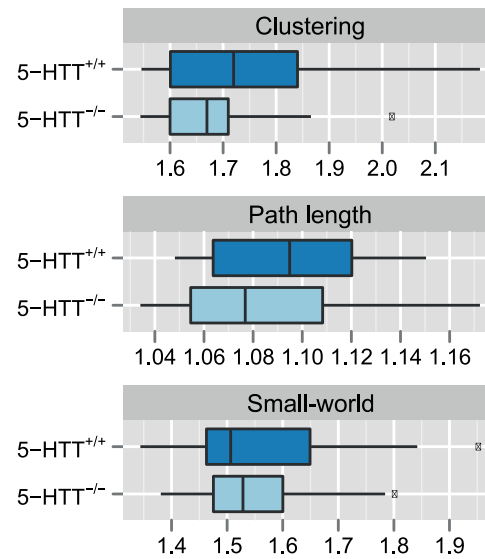doi:10.1371/journal.pone.0057780.g006

Figure 7. Network parameters from seed-based graph analysis of DTI tractography data. Structural brain networks were constructed from DTI-based fiber tracts among 23 bilaterally positioned cortical and subcortical gray matter ROIs. The edges between the regions were weighted by the mean fractional anisotropy along the tracts. The boxplots display three global network parameters that capture key properties of the networks: the clustering coefficient (i.e., average of local clustering coefficients), the characteristic path length (i.e., average of shortest path lengths), and the small-worldness (i.e., ratio of normalized clustering coefficient and normalized characteristic path length).
doi:10.1371/journal.pone.0057780.g007

but significant effect of 5-HTT genotype on fractional anisotropy values in the genu of the corpus callosum. This is consistent with the observation of lower fractional anisotropy values in the rostral body and genu of the corpus callosum, but not in other parts of the corpus callosum, in cocaine-dependent subjects, which paralleled impaired impulse control and reduced discriminability [77]. Furthermore, reductions in frontal white matter structural integrity have been reported in relation to 5-HTTLPR. Low 5-HTT expression has been associated with reduced fractional anisotropy along the frontal part of the uncinate fasciculus [78], and individual trait anxiety scores correlated negatively with fractional anisotropy along the pathway between amygdala and ventromedial prefrontal cortex [79]. The fractional anisotropy values in the corpus callosum of 5-HTT$^{+/+}$ rats are in agreement with estimates previously obtained in normally developing rats [80]. Lower fractional anisotropy in the genu of the corpus callosum might thus indicate that normal callosal axon myelination is disturbed in 5-HTT$^{-/-}$ rats, which may affect information integration across hemispheres. However, in the absence of histological data of callosal myelination that could provide support for the reductions in fractional anisotropy that we observed in the genu of the corpus callosum, and considering the potential contribution of fractional anisotropy values anterior to the corpus callosum due to partial-volume effects, one should be careful with interpretation.

Complex graph analysis measures of structural connectivity were not significantly different between 5-HTT$^{-/-}$ and 5-HTT$^{+/+}$ rats. However, these measures critically depend on the quality of the tractography results from which the underlying networks were

constructed. Considering the spatial resolution of whole-brain *in vivo* DTI, these connections are most likely to reflect shortest paths along major white matter tracts. Likewise, the estimates of fiber exit points into gray matter tissue are limited by partial volume effects along the borders between gray and white matter. In general, the sensitivity of DTI and BOLD-based fMRI measurements to detect genotype effects were dependent on the achieved contrasts and spatial resolutions. The BOLD-based pharmacological MRI contrast is small compared to the contrast afforded by exogenous agents, which could thus improve the detectability of small genotype effects [81]. Furthermore, the fMRI-signal is highly dependent on neurovascular coupling. Here, manganese-based tracing of neural connections could provide an alternative and independent mapping of functional connections [51]. Finally, DTI-based tractography could benefit from higher spatial resolutions achieved using *post mortem* MRI at ultra-high field strengths [82].

Except for a few species-specific effects of 5-HTT gene knockout and subtle differences that depend on the inbred mouse strain background, many reported (endo)phenotypes are highly similar for both 5-HTT$^{-/-}$ mice and rats (reviewed in [7,83]). Inbred 5-HTT knockout mice are generated using homologous recombination of embryonic stem cells [84,85], which only very recently became feasible in rats [86]. In contrast, the outbred 5-HTT$^{-/-}$ rat that was used in this study has been obtained through ENU-driven target-selected mutagenesis [87]. Whereas this approach may have left undetected mutations in other parts of the genome, the similarities with mouse knockouts suggests that the influence of any unknown additional mutation must be minimal. Complete absence of functional 5-HTT expression in 5-HTT$^{-/-}$ rodents may be perceived as an extreme condition, considering that 5-HTT function in s-allele carriers of 5-HTTLPR is reduced but not

absent [7,88]. Nevertheless, convergence of endophenotype effects of 5-HTT knockout in rodents and the similarities with brain and behavioral phenotypes in human s-allele carriers of 5-HTTLPR suggests that the use of 5-HTT$^{-/-}$ rodents may be helpful in understanding 5-HTT genotype effects on brain and behavior [8].

In the absence of functional 5-HTT expression in mice, functional and structural defects have been found in regions along pathways involved in somatosensory and visual processing [89–92]. It is tempting to speculate that the marginally significant increase in functional connectivity between the somatosensory cortex and insula contributes to the increased social cognition as proposed by Canli and Lesch [93], given that these regions are involved in interoceptive awareness and empathy [94]. Furthermore, the connectivity between the visual cortex, somatosensory cortex and ventromedial prefrontal cortex may serve as a pathway by which 5-HTT$^{-/-}$ rodents and 5-HTTLPR s-allele carriers engage into hypervigilance [8]. However, when considering the limited group sizes of the current study while multiple statistical tests of pairwise functional connectivity values were applied, control of the false discovery rate is appropriate and precludes conclusive acknowledgement of the aforementioned differences in functional connectivity.

In sum, our extensive MRI analysis of brain morphology and function in 5-HTT$^{-/-}$ versus wild-type rats reveals several new brain phenotypes. For instance, a decrease in fractional anisotropy in the genu of the corpus callosum was observed, which may imply that long-distance connectivity is altered in 5-HTT$^{-/-}$ rats, with potential consequences for the integration of information across hemispheres. Although the precise morphological nature and the functional implications remain to be identified, such a large-scale effect may contribute to multiple phenotypes as observed in 5-HTT$^{-/-}$ rats.

Acknowledgments

Author Contributions

Conceived and designed the experiments: JRH RMD. Performed the experiments: KvdM WMO. Analyzed the data: KvdM. Contributed reagents/materials/analysis tools: JRH WMO. Wrote the paper: KvdM JRH RMD.

References

1. Cools R, Roberts AC, Robbins TW (2008) Serotoninergic regulation of emotional and behavioural control processes. Trends Cogn Sci (Regul Ed) 12: 31–40. doi:10.1016/j.tics.2007.10.011.

2. Homberg JR (2012) Serotonin and decision making processes. Neurosci Biobehav Rev 36: 218–236. doi:10.1016/j.neubiorev.2011.06.001.

3. Margoob MA, Mushtaq D (2011) Serotonin transporter gene polymorphism and psychiatric disorders: Is there a link? Indian J Psychiatry 53: 289–299. doi:10.4103/0019-5545.91901.

4. Hariri AR, Holmes A (2006) Genetics of emotional regulation: the role of the serotonin transporter in neural function. Trends Cogn Sci (Regul Ed) 10: 182–191. doi:10.1016/j.tics.2006.02.011.

5. Lesch K-P, Bengel D, Heils A, Sabol SZ, Greenberg BD, et al. (1996) Association of anxiety-related traits with a polymorphism in the serotonin transporter gene regulatory region. Science 274: 1527–1531.

6. Caspi A, Sugden K, Moffitt TE, Taylor A, Craig IW, et al. (2003) Influence of life stress on depression: moderation by a polymorphism in the 5-HTT gene. Science 301: 386–389. doi:10.1126/science.1083968.

7. Kalueff AV, Olivier JDA, Nonkes LJP, Homberg JR (2010) Conserved role for the serotonin transporter gene in rat and mouse neurobehavioral endophenotypes. Neurosci Biobehav Rev 34: 373–386. doi:10.1016/j.neubiorev.2009.08.003.

8. Homberg JR, Lesch K-P (2011) Looking on the bright side of serotonin transporter gene variation. Biol Psychiatry 69: 513–519. doi:10.1016/j.biopsych.2010.09.024.

9. Nonkes LJP, Maes JHR, Homberg JR (2011) Improved cognitive flexibility in serotonin transporter knockout rats is unchanged following chronic cocaine self-administration. Addiction Biology: In press. doi:10.1111/j.1369-1600.2011.00351.x.

10. Homberg JR, De Boer SF, Raasø HS, Olivier JDA, Verheul M, et al. (2008) Adaptations in pre- and postsynaptic 5-HT1A receptor function and cocaine supersensitivity in serotonin transporter knockout rats. Psychopharmacology (Berl) 200: 367–380. doi:10.1007/s00213-008-1212-x.

11. Hall FS, Li X-F, Randall-Thompson J, Sora I, Murphy DL, et al. (2009) Cocaine-conditioned locomotion in dopamine transporter, norepinephrine transporter and 5-HT transporter knockout mice. Neuroscience 162: 870–880. doi:10.1016/j.neuroscience.2009.05.058.

12. Sora I, Wichems C, Takahashi N, Li XF, Zeng Z, et al. (1998) Cocaine reward models: conditioned place preference can be established in dopamine- and in serotonin-transporter knockout mice. Proc Natl Acad Sci USA 95: 7699–7704.

13. Sora I, Hall FS, Andrews AM, Itokawa M, Li XF, et al. (2001) Molecular mechanisms of cocaine reward. Combined dopamine and serotonin transporter knockouts eliminate cocaine place preference. Proceedings of the National Academy of Sciences USA 98: 5300–5305. doi:10.1073/pnas.091039298.

14. Nonkes LJP, van Bussel IPG, Verheij MMM, Homberg JR (2011) The interplay between brain 5-hydroxytryptamine levels and cocaine addiction. Behav Pharmacol 22: 723–738. doi:10.1097/FBP.0b013e32834d6260.

15. Koob GF (2009) Dynamics of neuronal circuits in addiction: reward, antireward, and emotional memory. Pharmacopsychiatry 42 Suppl 1: S32–41. doi:10.1055/s-0029-1216356.

16. Olivier JDA, Van Der Hart MGC, Van Swelm RPL, Dederen PJ, Homberg JR, et al. (2008) A study in male and female 5-HT transporter knockout rats: an animal model for anxiety and depression disorders. Neuroscience 152: 573–584. doi:10.1016/j.neuroscience.2007.12.032.

17. Pezawas L, Meyer-Lindenberg A, Drabant EM, Verchinski BA, Munoz KE, et al. (2005) 5-HTTLPR polymorphism impacts human cingulate-amygdala interactions: a genetic susceptibility mechanism for depression. Nat Neurosci 8: 828–834. doi:10.1038/nn1463.

18. Hariri AR, Tessitore A, Mattay VS, Fera F, Weinberger DR (2002) The amygdala response to emotional stimuli: a comparison of faces and scenes. Neuroimage 17: 317–323.

19. Wellman CL, Izquierdo A, Garrett JE, Martin KP, Carroll J, et al. (2007) Impaired stress-coping and fear extinction and abnormal corticolimbic morphology in serotonin transporter knock-out mice. J Neurosci 27: 684–691. doi:10.1523/JNEUROSCI.4595-06.2007.

20. Nietzer SL, Bonn M, Jansen F, Heiming RS, Lewejohann L, et al. (2011) Serotonin transporter knockout and repeated social defeat stress: impact on neuronal morphology and plasticity in limbic brain areas. Behav Brain Res 220: 42–54. doi:10.1016/j.bbr.2011.01.011.

21. Bearer EL, Zhang X, Janvelyan D, Boulat B, Jacobs RE (2009) Reward circuitry is perturbed in the absence of the serotonin transporter. Neuroimage 46: 1091–1104. doi:10.1016/j.neuroimage.2009.03.026.

22. Tuch DS, Reese TG, Wiegell MR, Makris N, Belliveau JW, et al. (2002) High angular resolution diffusion imaging reveals intravoxel white matter fiber heterogeneity. Magn Reson Med 48: 577–582. doi:10.1002/mrm.10268.

23. Avants BB, Tustison NJ, Song G, Cook PA, Klein A, et al. (2011) A reproducible evaluation of ANTs similarity metric performance in brain image registration. Neuroimage 54: 2033–2044. doi:10.1016/j.neuroimage.2010.09.025.

24. Paxinos G, Watson C (2005) The rat brain in stereotaxic coordinates. Burlington: Elsevier Academic Press.

25. Jenkinson M, Bannister P, Brady M, Smith S (2002) Improved optimization for the robust and accurate linear registration and motion correction of brain images. Neuroimage 17: 825–841.

26. Weissenbacher A, Kasess C, Gerstl F, Lanzenberger R, Moser E, et al. (2009) Correlations and anticorrelations in resting-state functional connectivity MRI: a quantitative comparison of preprocessing strategies. Neuroimage 47: 1408–1416. doi:10.1016/j.neuroimage.2009.05.005.

27. Wang R, Benner T, Sorensen AG, Wedeen VJ (2007) Diffusion Toolkit: A Software Package for Diffusion Imaging Data Processing and Tractography. Proc. Intl. Soc. Mag. Reson. Med. Berlin, Germany, Vol. 15. p. 3720.

28. Heidbreder CA, Groenewegen HJ (2003) The medial prefrontal cortex in the rat: evidence for a dorso-ventral distinction based upon functional and anatomical characteristics. Neurosci Biobehav Rev 27: 555–579.

29. Uylings HBM, Groenewegen HJ, Kolb B (2003) Do rats have a prefrontal cortex? Behav Brain Res 146: 3–17.

30. Ward BD (2000) Simultaneous inference for fMRI data. Available: http://afni.nimh.nih.gov/afni/doc/manual/AlphaSim. Accessed 31 January 2013.

31. Cox RW (1996) AFNI: software for analysis and visualization of functional magnetic resonance neuroimages. Comput Biomed Res 29: 162–173.

32. Stam CJ, Reijneveld JC (2007) Graph theoretical analysis of complex networks in the brain. Nonlinear Biomed Phys 1: 3. doi:10.1186/1753-4631-1-3.

33. Bullmore E, Sporns O (2009) Complex brain networks: graph theoretical analysis of structural and functional systems. Nat Rev Neurosci 10: 186–198. doi:10.1038/nrn2575.

34. Rubinov M, Sporns O (2010) Complex network measures of brain connectivity: uses and interpretations. Neuroimage 52: 1059–1069. doi:10.1016/j.neuroimage.2009.10.003.

35. Bullmore E, Sporns O (2012) The economy of brain network organization. Nat Rev Neurosci 13: 336–349. doi:10.1038/nrn3214.

36. Csardi G, Nepusz T (2006) The igraph software package for complex network research. InterJournal Complex Systems: 1695.

37. Onnela J-P, Saramäki J, Kertész J, Kaski K (2005) Intensity and coherence of motifs in weighted complex networks. Phys Rev E Stat Nonlin Soft Matter Phys 71: 065103.

38. Ponten SC, Douw L, Bartolomei F, Reijneveld JC, Stam CJ (2009) Indications for network regularization during absence seizures: weighted and unweighted graph theoretical analyses. Exp Neurol 217: 197–204. doi:10.1016/j.expneurol.2009.02.001.

39. Watts DJ, Strogatz SH (1998) Collective dynamics of "small-world" networks. Nature 393: 440–442. doi:10.1038/30918.

40. Bassett DS, Bullmore E (2006) Small-world brain networks. Neuroscientist 12: 512–523. doi:10.1177/1073858406293182.

41. Stam CJ, de Haan W, Daffertshofer A, Jones BF, Manshanden I, et al. (2009) Graph theoretical analysis of magnetoencephalographic functional connectivity in Alzheimer's disease. Brain 132: 213–224. doi:10.1093/brain/awn262.

42. Pinheiro J, Bates D, DebRoy S, Sarkar D, R Development Core Team (2012) nlme: Linear and Nonlinear Mixed Effects Models.

43. Plummer M (2003) JAGS: A program for analysis of Bayesian graphical models using Gibbs sampling. Proceedings of the 3rd International Workshop on Distributed Statistical Computing (DSC 2003); March 20-22; Vienna, Austria.

44. Pendse GV, Schwarz AJ, Baumgartner R, Coimbra A, Upadhyay J, et al. (2010) Robust, unbiased general linear model estimation of phMRI signal amplitude in the presence of variation in the temporal response profile. J Magn Reson Imaging 31: 1445–1457. doi:10.1002/jmri.22180.

45. Donders ART, van der Heijden GJMG, Stijnen T, Moons KGM (2006) Review: a gentle introduction to imputation of missing values. J Clin Epidemiol 59: 1087–1091. doi:10.1016/j.jclinepi.2006.01.014.

46. Smith SM, Jenkinson M, Johansen-Berg H, Rueckert D, Nichols TE, et al. (2006) Tract-based spatial statistics. Voxelwise analysis of multi-subject diffusion data. NeuroImage 31: 1487–1505. doi:10.1016/j.neuroimage.2006.02.024.

47. Lira A, Zhou M, Castanon N, Ansorge MS, Gordon JA, et al. (2003) Altered depression-related behaviors and functional changes in the dorsal raphe nucleus of serotonin transporter-deficient mice. Biol Psychiatry 54: 960–971.

48. Holmes A, Lit Q, Murphy DL, Gold E, Crawley JN (2003) Abnormal anxiety-related behavior in serotonin transporter null mutant mice: the influence of genetic background. Genes Brain Behav 2: 365–380.

49. Holmes A, Yang RJ, Lesch K-P, Crawley JN, Murphy DL (2003) Mice lacking the serotonin transporter exhibit 5-HT(1A) receptor-mediated abnormalities in tests for anxiety-like behavior. Neuropsychopharmacology 28: 2077–2088. doi:10.1038/sj.npp.1300266.

50. Pautler RG, Silva AC, Koretsky AP (1998) In vivo neuronal tract tracing using manganese-enhanced magnetic resonance imaging. Magn Reson Med 40: 740–748.

51. Silva AC, Lee JH, Aoki I, Koretsky AP (2004) Manganese-enhanced magnetic resonance imaging (MEMRI): methodological and practical considerations. NMR Biomed 17: 532–543. doi:10.1002/nbm.945.

52. Bearer EL, Falzone TL, Zhang X, Biris O, Rasin A, et al. (2007) Role of neuronal activity and kinesin on tract tracing by manganese-enhanced MRI (MEMRI). Neuroimage 37 Suppl 1: S37–46. doi:10.1016/j.neuroimage.2007.04.053.

53. Lowe AS, Thompson ID, Sibson NR (2008) Quantitative manganese tract tracing: dose-dependent and activity-independent terminal labelling in the mouse visual system. NMR Biomed 21: 859–867. doi:10.1002/nbm.1272.

54. Damoiseaux JS, Greicius MD (2009) Greater than the sum of its parts: a review of studies combining structural connectivity and resting-state functional connectivity. Brain Struct Funct 213: 525–533. doi:10.1007/s00429-009-0208-6.

55. Honey CJ, Sporns O, Cammoun L, Gigandet X, Thiran JP, et al. (2009) Predicting human resting-state functional connectivity from structural connectivity. Proc Natl Acad Sci U S A 106: 2035–2040. doi:10.1073/pnas.0811168106.

56. Hariri AR, Mattay VS, Tessitore A, Kolachana B, Fera F, et al. (2002) Serotonin transporter genetic variation and the response of the human amygdala. Science 297: 400–403. doi:10.1126/science.1071829.

57. Munafò MR, Brown SM, Hariri AR (2008) Serotonin transporter (5-HTTLPR) genotype and amygdala activation: a meta-analysis. Biol Psychiatry 63: 852–857. doi:10.1016/j.biopsych.2007.08.016.

58. Heinz A, Braus DF, Smolka MN, Wrase J, Puls I, et al. (2005) Amygdala-prefrontal coupling depends on a genetic variation of the serotonin transporter. Nat Neurosci 8: 20–21. doi:10.1038/nn1366.

59. Canli T, Omura K, Haas BW, Fallgatter A, Constable RT, et al. (2005) Beyond affect: a role for genetic variation of the serotonin transporter in neural activation during a cognitive attention task. Proc Natl Acad Sci USA 102: 12224–12229. doi:10.1073/pnas.0503880102.

60. Lee T-W, Yu YWY, Hong C-J, Tsai S-J, Wu H-C, et al. (2011) The influence of serotonin transporter polymorphisms on cortical activity: a resting EEG study. BMC Neurosci 12: 33. doi:10.1186/1471-2202-12-33.

61. Canli T, Qiu M, Omura K, Congdon E, Haas BW, et al. (2006) Neural correlates of epigenesis. Proc Natl Acad Sci USA 103: 16033–16038. doi:10.1073/pnas.0601674103.

62. Rao H, Gillihan SJ, Wang J, Korczykowski M, Sankoorikal GMV, et al. (2007) Genetic variation in serotonin transporter alters resting brain function in healthy individuals. Biol Psychiatry 62: 600–606. doi:10.1016/j.biopsych.2006.11.028.

63. Viviani R, Sim E-J, Lo H, Beschoner P, Osterfeld N, et al. (2010) Baseline brain perfusion and the serotonin transporter promoter polymorphism. Biol Psychiatry 67: 317–322. doi:10.1016/j.biopsych.2009.08.035.

64. Gokturk C, Schultze S, Nilsson KW, von Knorring L, Oreland L, et al. (2008) Serotonin transporter (5-HTTLPR) and monoamine oxidase (MAOA) promoter polymorphisms in women with severe alcoholism. Arch Womens Ment Health 11: 347–355. doi:10.1007/s00737-008-0033-6.

65. Enoch M-A, Gorodetsky E, Hodgkinson C, Roy A, Goldman D (2011) Functional genetic variants that increase synaptic serotonin and 5-HT3 receptor sensitivity predict alcohol and drug dependence. Mol Psychiatry 16: 1139–1146. doi:10.1038/mp.2010.94.

66. Gerra G, Zaimovic A, Garofano L, Ciusa F, Moi G, et al. (2007) Perceived parenting behavior in the childhood of cocaine users: relationship with genotype and personality traits. Am J Med Genet B Neuropsychiatr Genet 144B: 52–57. doi:10.1002/ajmg.b.30388.

67. Ritz MC, Cone EJ, Kuhar MJ (1990) Cocaine inhibition of ligand binding at dopamine, norepinephrine and serotonin transporters: a structure-activity study. Life Sci 46: 635–645.

68. Tsukada H, Nishiyama S, Kakiuchi T, Ohba H, Sato K, et al. (1999) Isoflurane anesthesia enhances the inhibitory effects of cocaine and GBR12909 on dopamine transporter: PET studies in combination with microdialysis in the monkey brain. Brain Res 849: 85–96.

69. Byas-Smith MG, Li J, Szlam F, Eaton DC, Votaw JR, et al. (2004) Isoflurane induces dopamine transporter trafficking into the cell cytoplasm. Synapse 53: 68–73. doi:10.1002/syn.20037.

70. Whittington RA, Virág L (2006) Isoflurane decreases extracellular serotonin in the mouse hippocampus. Anesth Analg 103: 92–98. doi:10.1213/01.ane.0000221488.48352.61.

71. Martin DC, Adams RJ, Aronstam RS (1990) The influence of isoflurane on the synaptic activity of 5-hydroxytryptamine. Neurochem Res 15: 969–973.

72. Masamoto K, Kim T, Fukuda M, Wang P, Kim S-G (2007) Relationship between neural, vascular, and BOLD signals in isoflurane-anesthetized rat somatosensory cortex. Cereb Cortex 17: 942–950. doi:10.1093/cercor/bhl005.

73. Du C, Tully M, Volkow ND, Schiffer WK, Yu M, et al. (2009) Differential effects of anesthetics on cocaine's pharmacokinetic and pharmacodynamic effects in brain. Eur J Neurosci 30: 1565–1575. doi:10.1111/j.1460-9568.2009.06931.x.

74. Reyes-Haro D, García-Alcocer G, Miledi R, García-Colunga J (2003) Uptake of serotonin by adult rat corpus callosum is partially reduced by common antidepressants. J Neurosci Res 74: 97–102. doi:10.1002/jnr.10724.

75. Simpson KL, Weaver KJ, de Villers-Sidani E, Lu JY-F, Cai Z, et al. (2011) Perinatal antidepressant exposure alters cortical network function in rodents. Proc Natl Acad Sci USA 108: 18465–18470. doi:10.1073/pnas.1109353108.

76. Ansorge MS, Zhou M, Lira A, Hen R, Gingrich JA (2004) Early-life blockade of the 5-HT transporter alters emotional behavior in adult mice. Science 306: 879–881. doi:10.1126/science.1101678.

77. Moeller FG, Hasan KM, Steinberg JL, Kramer LA, Dougherty DM, et al. (2005) Reduced anterior corpus callosum white matter integrity is related to increased impulsivity and reduced discriminability in cocaine-dependent subjects: diffusion tensor imaging. Neuropsychopharmacology 30: 610–617. doi:10.1038/sj.npp.1300617.

78. Pacheco J, Beevers CG, Benavides C, McGeary J, Stice E, et al. (2009) Frontal-limbic white matter pathway associations with the serotonin transporter gene promoter region (5-HTTLPR) polymorphism. J Neurosci 29: 6229–6233. doi:10.1523/JNEUROSCI.0896-09.2009.

79. Kim MJ, Whalen PJ (2009) The structural integrity of an amygdala-prefrontal pathway predicts trait anxiety. J Neurosci 29: 11614–11618. doi:10.1523/JNEUROSCI.2335-09.2009.

80. Bockhorst KH, Narayana PA, Liu R, Ahobila-Vijjula P, Ramu J, et al. (2008) Early postnatal development of rat brain: in vivo diffusion tensor imaging. J Neurosci Res 86: 1520–1528. doi:10.1002/jnr.21607.

81. Mandeville JB, Jenkins BG, Chen Y-CI, Choi J-K, Kim YR, et al. (2004) Exogenous contrast agent improves sensitivity of gradient-echo functional magnetic resonance imaging at 9.4 T. Magn Reson Med 52: 1272–1281. doi:10.1002/mrm.20278.

82. Zhang J, Miller MI, Plachez C, Richards LJ, Yarowsky P, et al. (2005) Mapping postnatal mouse brain development with diffusion tensor microimaging. NeuroImage 26: 1042–1051. doi:10.1016/j.neuroimage.2005.03.009.

83. Olivier JDA, Cools AR, Ellenbroek BA, Cuppen E, Homberg JR (2010) The serotonin transporter knock-out rat: a review. In: Kalueff AV, LaPorte JL, editors. Experimental Models in Serotonin Transporter Research. Cambridge University Press. pp. 170–213. doi:10.1017/CBO9780511729935.

84. Capecchi MR (1989) Altering the genome by homologous recombination. Science 244: 1288–1292.

85. Bengel D, Murphy DL, Andrews AM, Wichems CH, Feltner D, et al. (1998) Altered brain serotonin homeostasis and locomotor insensitivity to 3, 4-methylenedioxymethamphetamine ("Ecstasy") in serotonin transporter-deficient mice. Mol Pharmacol 53: 649–655.

86. Tong C, Li P, Wu NL, Yan Y, Ying Q-L (2010) Production of p53 gene knockout rats by homologous recombination in embryonic stem cells. Nature 467: 211–213. doi:10.1038/nature09368.

87. Smits BMG, Mudde JB, van de Belt J, Verheul M, Olivier J, et al. (2006) Generation of gene knockouts and mutant models in the laboratory rat by ENU-driven target-selected mutagenesis. Pharmacogenet Genomics 16: 159–169. doi:10.1097/01.fpc.0000184960.82903.8f.

88. Kalueff AV, Ren-Patterson RF, Murphy DL (2007) The developing use of heterozygous mutant mouse models in brain monoamine transporter research. Trends Pharmacol Sci 28: 122–127. doi:10.1016/j.tips.2007.01.002.

89. Esaki T, Cook M, Shimoji K, Murphy DL, Sokoloff L, et al. (2005) Developmental disruption of serotonin transporter function impairs cerebral responses to whisker stimulation in mice. Proc Natl Acad Sci USA 102: 5582–5587. doi:10.1073/pnas.0501509102.

90. Altamura C, Dell'Acqua ML, Moessner R, Murphy DL, Lesch KP, et al. (2007) Altered neocortical cell density and layer thickness in serotonin transporter knockout mice: a quantitation study. Cereb Cortex 17: 1394–1401. doi:10.1093/cercor/bhl051.

91. Pang RD, Wang Z, Klosinski LP, Guo Y, Herman DH, et al. (2011) Mapping functional brain activation using [C]-iodoantipyrine in male serotonin transporter knockout mice. PLoS ONE 6: e23869. doi:10.1371/journal.pone.0023869.

92. Upton AL, Ravary A, Salichon N, Moessner R, Lesch K-P, et al. (2002) Lack of 5-HT(1B) receptor and of serotonin transporter have different effects on the segregation of retinal axons in the lateral geniculate nucleus compared to the superior colliculus. Neuroscience 111: 597–610.

93. Canli T, Lesch K-P (2007) Long story short: the serotonin transporter in emotion regulation and social cognition. Nat Neurosci 10: 1103–1109. doi:10.1038/nn1964.

94. Olsson A, Nearing KI, Phelps EA (2007) Learning fears by observing others: the neural systems of social fear transmission. Soc Cogn Affect Neurosci 2: 3–11. doi:10.1093/scan/nsm005.